

# FORTE – a multipurpose high-vacuum diffractometer for tender X-ray diffraction and spectroscopy at the SIRIUS beamline of Synchrotron SOLEIL

G. Ciatto,<sup>a\*</sup> N. Aubert,<sup>a</sup> M. Lecroard,<sup>a</sup> C. Engblom,<sup>a</sup> P. Fontaine,<sup>a</sup> J.-M. Dubuisson,<sup>a</sup> Y.-M. Abiven,<sup>a</sup> P.-E. Janolin,<sup>b</sup> J.-M. Kiat,<sup>b‡</sup> Y. Dumont,<sup>c</sup> B. Berini,<sup>c</sup> A. Fouchet<sup>c§</sup> and N. Keller<sup>c</sup>

Received 15 January 2019

Accepted 18 March 2019

Edited by Y. Amemiya, University of Tokyo, Japan

‡ Deceased.

§ Present address: Laboratoire de Cristallographie et Sciences des Matériaux (CRISMAT), Université de Caen Normandie CNRS-ENSI-CAEN, Caen, France.

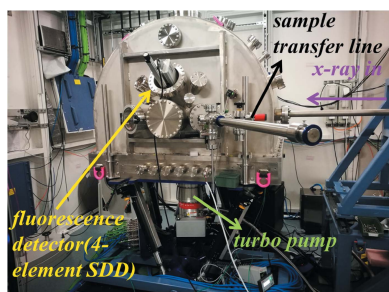
**Keywords:** diffractometers; tender X-rays; diffraction anomalous fine structure (DAFS); X-ray absorption (XAS); functional oxides.

<sup>a</sup>Synchrotron SOLEIL, L'Orme des Merisiers, Saint-Aubin, BP 48 F-91192 Gif sur Yvette CEDEX, France, <sup>b</sup>Laboratoire SPMS, UMR CNRS-CentraleSupélec, Bâtiment Gustave Eiffel – MB.105, 8–10 rue Joliot-Curie, 91190 Gif-Sur-Yvette CEDEX, France, and <sup>c</sup>Groupe d'Etudes de la Matière Condensée (GEMaC), Université Versailles Saint-Quentin en Yvelines – CNRS, Université Paris-Saclay, Versailles, France. \*Correspondence e-mail: gianluca.ciatto@synchrotron-soleil.fr

A new high-vacuum multipurpose diffractometer (called FORTE from the French acronyms of the project) has recently been installed at the tender/hard X-ray SIRIUS beamline of Synchrotron SOLEIL, France. The geometry chosen allows one to work either in the classical Eulerian four-circle geometry for bulk X-ray diffraction (XRD) or in the  $z$ -axis geometry for surface XRD. The diffractometer nicely fits the characteristics of the SIRIUS beamline, optimized to work in the 1.1–4.5 keV range, and allows one to perform unprecedented diffraction anomalous fine structure (DAFS) experiments in the tender X-ray region, also around non-specular reflections, covering a large reciprocal-space volume. Installation of an X-ray fluorescence detector on a dedicated flange allows simultaneous DAFS and X-ray absorption (XAS) measurements. The access to the tender X-ray region paves the way to resonant investigations around the  $L$ -edges of second-row transition elements which are constituents of functional oxide materials. It also enables access to several edges of interest for semiconductors. Finally, the control architecture based on synchronized Delta Tau units opens up exciting perspectives for improvement of the mechanical sphere of confusion.

## 1. Introduction

X-ray diffraction (XRD) is still one of the most commonly used structural characterization techniques in synchrotron radiation facilities worldwide and free-electron lasers; it is applied in a variety of scientific areas ranging from fundamental physics (McBride *et al.*, 2019) to biology (Nemoz *et al.*, 2018), from materials science (Huang *et al.*, 2015) to cultural heritage (Bao *et al.*, 2018). The diversity in users' demands has driven the development of the most suitable instrumentation for specific applications, *e.g.* diffractometers with robotic sample-changer systems and fast alignment tools for macromolecular crystallography beamlines (Fuchs *et al.*, 2014), many-circle diffractometers for precise alignment of crystals in materials science (Seeck *et al.*, 2012; Nowak *et al.*, 2006), ultra high vacuum (UHV) instruments for reactive surface studies (Nicklin *et al.*, 2016; Fuoss & Robinson, 1984) and specific setups for liquids (Smilgies *et al.*, 2005; Murphy *et al.*, 2014; Fontaine *et al.*, 2014). Recently, the upgrade programme that several synchrotrons have planned for lowering the emittance via the use of multi-bend achromat (MBA) storage rings (Einfeld, 2014) is boosting the design of diffractometers with



© 2019 International Union of Crystallography

sub-micrometre positional stability and reproducibility in order to benefit from the enhanced coherence of the future X-ray beams (Ju *et al.*, 2017). Synchrotron beamlines often welcome different kinds of experiments and sample environments, and thus the versatility of the setup is also a very important criterion to be taken into account when building a diffractometer (Dyadkin *et al.*, 2016).

When working in the hard X-ray region, absorption by air and windows is usually not a big issue in diffractometer design: the detector can be mounted out of the sample chamber (if any chamber exists), most of the positioning motors work in air, reducing the risk of overheating and sample pollution, and space constraints are often less severe. Several geometries, using as many circles as necessary for the experimental applications, have been devised in order to cover the available reciprocal space (Bunk & Nielsen, 2004; Vlieg, 1998; Lohmeier & Vlieg, 1993; Thorkildsen *et al.*, 1999). Diffractometers hosting stations for *in situ* sample growth and characterization exploit the high brilliance and time structure of modern synchrotron radiation facilities (Lee *et al.*, 2016; Boichot *et al.*, 2016). However, in hard X-ray beamlines, due to the presence of beryllium (or other) windows and the use of double-crystal monochromators equipped with Si crystals, there is little possibility of performing resonant scattering and diffraction below 3 keV (Stempfer *et al.*, 2013).

In the soft X-ray region, instead, absorption by air is dramatic and the detector (with ultra-thin windows or windowless) has to be inserted in the vacuum chamber. When the sample needs to be measured at low temperature, contamination is an issue because the sample can act as a cold finger in the case of scarce vacuum level and contamination layers deposited on the sample surface can absorb an important fraction of the soft X-rays. This is the reason why several soft X-ray diffractometers/reflectometers were built by minimizing the number of in-vacuum motors in order to reach the UHV level. UHV is also necessary when the surface is sensitive and can react with residual water vapours in the chamber; this is the case, for example, for ferroelectric oxides, where the dissociative adsorption of water can act as an extrinsic mechanism for screening the surface polarization charge. A typical strategy frequently exploited in soft X-ray beamlines is to choose a horizontal scattering geometry with sample actuation and detector rotation kept outside of the vacuum chamber, with the motion being transmitted through bellows and a differential-pumped rotary seal (Jaouen *et al.*, 2004; Grabis *et al.*, 2003; Brück *et al.*, 2008; Staub *et al.*, 2008; Takeuchi *et al.*, 2009). These soft X-ray diffractometers/reflectometers are normally provided with an azimuthal angle ( $\phi$ ) covering a large range, either manual or motorized, and a very limited (a few degrees) tilt angle ( $\chi$ ). Polarization is switched using the undulator source and without moving the sample. The degrees of freedom provided by this modified reflectometer geometry, considering also the strong contraction of reciprocal space in the soft X-ray region, are sufficient to address the study of charge, magnetic and orbit ordering in several scientific cases, especially probing the magnetically active 3d electron band of first-row transition metals. In other

soft X-ray reflectometers/diffractometers, a vertical scattering configuration is chosen to benefit from the low divergence of the beam (Beale *et al.*, 2010); in fewer examples the geometry features in-vacuum motors (Hawthorn *et al.*, 2011; Beutier *et al.*, 2007) or is aimed at integrating several experimental methods within the same sample environment (Abrudan *et al.*, 2015), sometimes compromising with the UHV vacuum level.

In the tender X-ray region (arguably, the 1–5 keV range), the requirements of hard X-rays and the issues intrinsic to soft X-rays overlap: on the one hand, the use of windows and (even) short sections in air is inconvenient due to the rather strong absorption; on the other hand, several crystal plane reflections become available, depending on the material under study, and this calls for a larger covering of reciprocal space (*i.e.* a more extended range for the diffractometer circles) and better angular resolution to measure the XRD peaks. Because of these difficulties, the tender X-ray energy range has historically been less exploited by XRD synchrotron beamlines worldwide, even for resonant studies. In addition, spectroscopy beamlines often have difficulties in covering the tender X-ray energy range too, it being located just between the two working ranges of the application of classical grating and double-crystal monochromators. Nevertheless, there is tremendous interest in performing both resonant scattering/diffraction investigations and spectroscopy in the tender X-ray region. In fact, this energy range encompasses the *L*-edges of second-row transition elements (Sr, Y, Zr, Nb, Ru, Mo *etc.*), which are constituents of functional oxide materials, and also hosts several edges of interest for semiconductors (Al, Si, P, In, Sb *etc.*).

In this paper we present a new multipurpose high-vacuum (HV) diffractometer optimized to perform both XRD and spectroscopy in the tender X-ray region. The HV diffractometer has recently been installed at the SIRIUS beamline of Synchrotron SOLEIL and showcases its innovative multilayer grating-based optics and undulator source. The design and geometry have been devised as a compromise between technical and users' requirements, versatility and vacuum level. This new end-station allows us to perform high-quality diffraction anomalous fine structure (DAFS) experiments in the tender X-ray region, also around non-specular reflections, covering a large reciprocal-space volume. It enables simultaneous DAFS and X-ray absorption (XAS) measurements in addition to resonant X-ray reflectivity (XRR) and tender X-ray grazing-incidence small-angle scattering (GISAXS). Moreover, the instrument will benefit from the characteristics of the upgraded SOLEIL ring for coherent diffraction imaging (CDI). The HV diffractometer was manufactured and assembled by the Symétrie company (Nîmes, France) and founded by two parallel projects: a joint agreement with the Swedish MAX IV Synchrotron [a twin prototype is being installed at the FemtoMAX beamline (Enquist *et al.*, 2018)] and a regional project, the Île-de-France DIM OXYMORE project 'FORTE' (from the French acronym), which also gave its name to the end-station. In the next section we will give a brief description of the main characteristics of the SIRIUS beamline; in Section 3 we will present the geometry, mechanics

and performance of the diffractometer including available detectors, sample environment and control system; in Section 4 we will present selected results of the first commissioning and collaborative experiments performed with the end-station; finally, in Section 5 we will draw a possible upgrade path for the near future, before concluding.

## 2. The SIRIUS beamline

The SIRIUS beamline has already been described in two recent papers (Ciatto *et al.*, 2016; Fontaine *et al.*, 2014) and we refer readers to those references for a detailed presentation. Here, we limit ourselves to providing a summary of the most important features that are key for the use of the FORTE diffractometer, which constitutes one of the SIRIUS end-stations.

SIRIUS is mounted on a helicoidal Apple-II undulator X-ray source with 36 mm magnetic period (HU36) (Kitegi *et al.*, 2010) which provides variable polarization (linear vertical, linear horizontal and circular) and it is equipped with two monochromators mounted in series and used alternately. The first is a double-crystal monochromator (DCM) at a distance of 18.5 m from the source which uses a pair of liquid nitrogen cooled Si [111] crystals; the second is a multilayer-grating monochromator (MGM) consisting of a variable line spaced holographic diffraction grating with line density of 2400 lines  $\text{mm}^{-1}$  over which a multilayer with 35 periods of Cr (2.5 nm)/B<sub>4</sub>C (4.1 nm) has been deposited, and two matched multilayer mirrors as a second optical element. The two monochromators are followed by a set of four mirrors which provide high harmonics rejection, focusing of the beam in the vertical and horizontal plane, and optional beam deflection. The smallest beam spot on the sample at the end-stations in focused mode (without flux reduction) is about 0.1 mm  $\times$  0.05 mm [vertical (V)  $\times$  horizontal (H)] and four positions of the beam at the end-station level are possible, depending on whether or not the mirrors are used, and, if they are used, on the specific mirror combination.

Although the beamline provides photons in a continuous energy range of 1.1–13 keV using either one or the other monochromator and is also routinely exploited for hard X-ray studies, its range of excellence is the tender X-ray region, where the MGM is used. This range matches the highest-performance region of the SOLEIL ring. The MGM, which works in combination with an elliptic mirror focusing on an energy-selecting slit (ESS), provides high flux and good energy resolution in the 1.1–4.5 keV energy range. Moreover, it preserves circular polarization in this range, which would not be possible with the DCM since the Brewster angle for Si [111] is located around 2.8 keV. As a consequence, the MGM can also be used for X-ray magnetic circular dichroism (XMCD) and X-ray resonant magnetic scattering (XRMS) experiments in the tender X-ray region. The performances of the MGM are shown in Fig. 1 where the X-ray flux at the end-station level is plotted as a function of energy for a typical high-energy-resolution configuration used for spectroscopy at grazing incidence. Here the beam is focused only vertically and the

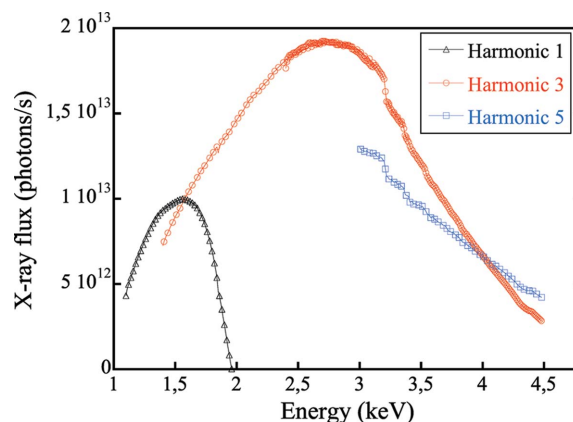


**Figure 1**  
X-ray flux impinging on the sample as a function of the energy in a typical configuration of the SIRIUS beamline using the MGM and the first three harmonics of the HU36 undulator.

ESS is rather closed (5  $\mu\text{m}$ ); the X-ray flux has been measured by using an ultra-thin optical-grade diamond membrane specifically designed for monitoring the beam intensity/position and for normalizing spectra at the SIRIUS beamline (Desjardins *et al.*, 2014). Fig. 1 shows that, switching between the harmonics 1, 3 and 5 of the HU36 undulator, the X-ray flux can always be maintained above  $4 \times 10^{12}$  photons  $\text{s}^{-1}$  in the 1.1–4.5 keV energy range and it reaches almost the level of  $2 \times 10^{13}$  photons  $\text{s}^{-1}$  in the 2.5–3 keV range. Energy resolution ( $\Delta E/E$ ) is between  $1.5 \times 10^{-4}$  and  $2 \times 10^{-4}$  in the MGM energy range for the ESS opening chosen in Fig. 1, close to the resolution offered by a Si [111] DCM and more than sufficient for application in XAS and DAFS spectroscopies. Flux can be raised above  $3 \times 10^{13}$  by opening the ESS and accepting a lower energy resolution; such X-ray fluxes in the tender X-ray region are rather impressive for a grating-based technology. More technical details about the MGM will be published in a dedicated paper currently in preparation.

The HV diffractometer that will be described in the following sections is one of two end-stations available at the SIRIUS beamline; the other end-station is a large seven-circle diffractometer which can be used either with a ‘kappa head’ goniometer (Thorkildsen *et al.*, 1999), on which a baby chamber can be mounted, or with a six-axis tower for heavy and cumbersome sample environments. Although there is no restriction in using the FORTE diffractometer in the hard X-ray energy range up to 13 keV, the use of the other end-station is more convenient in that range. In fact, when the use of Be windows to separate vacuum and air sections does not represent a limit, the seven-circle diffractometer allows one to mount larger sample environments and detectors, to select longer sample–detector distances when necessary and to switch the samples faster.

## 3. The high-vacuum diffractometer

### 3.1. Geometry

A conceptual sketch of the FORTE diffractometer geometry is shown in Fig. 2. The instrument consists of a four-

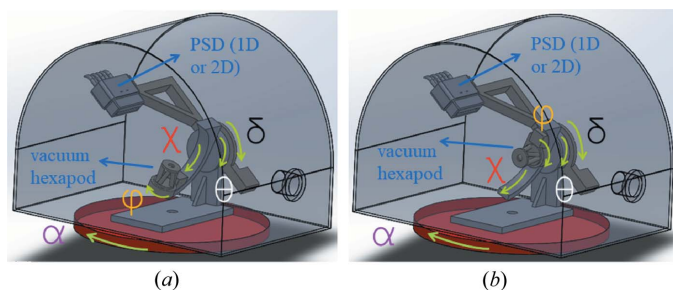


**Figure 2**  
Sketch of the HV diffractometer geometry. (a) Four-circle configuration for bulk XRD; (b) configuration for surface XRD.

circle Eulerian diffractometer with full-range  $\theta$ ,  $\delta$ ,  $\phi$  circles and a rather extended  $\chi$  circle (more than  $100^\circ$ ) incorporated in a vacuum chamber, plus an additional vertical axis rotation ( $\alpha$ ) of the whole vessel ( $\pm 10^\circ$ ). The latter rotation is external to the vacuum vessel, and the connection of the vessel to the beamline requires the use of a bellow which can withstand movements about the  $\alpha$  arc. This choice allows one to work either in a classical four-circle geometry (Busing & Levy, 1967) for bulk XRD [Fig. 2(a)] or in a configuration similar to the  $z$ -axis geometry (Bloch, 1985; Feidenhans'l, 1989) for surface XRD, with the second detector circle replaced by a position-sensitive detector (PSD) mounted on the  $\delta$  arm. In the latter configuration [Fig. 2(b)], the sample surface is vertical ( $\chi = 90^\circ$ ),  $\alpha$  is used to set (or scan) the incidence angle and a precise alignment of the sample surface normal with the  $\phi$  rotation axis is possible by using an in-vacuum hexapod mounted on the  $\phi$  circle.

This geometry choice offers the following advantages:

(i) The absence of Be windows allows direct connection to the storage ring vacuum, enabling experiments down to an energy as low as 1.1 keV.

(ii) The use of a very open  $\chi$  circle, analogously to a kappa geometry, leaves enough space on the side opposite to the mechanics for the installation of ancillary instrumentation (e.g. fluorescence X-ray detectors).

(iii) The  $\chi$  range is sufficiently wide to allow access to non-specular reflections which would not be accessible in a reflectometer geometry. To give an idea of the reciprocal-space volume covered, in Table 1 we list the crystal plane reflections reachable in resonant conditions for two case studies: a strained  $\text{In}_{0.38}\text{Ga}_{0.62}\text{As}$  semiconductor pseudomorphic on GaAs substrate (tetragonal distortion of a zinc-blende cell) analysed at the In  $L_3$ -edge and a  $\text{PbSc}_{0.5}\text{Nb}_{0.5}\text{O}_3$  relaxor oxide (trigonal, but approximable as a cubic perovskite) studied at the Nb  $L_3$ -edge. The two edges are located in the tender X-ray region, at 3.730 and 2.371 keV, respectively.

(iv) The possibility of working in either vertical or horizontal scattering geometry provides high versatility in addressing the different user demands. In particular, FORTE allows the use of grazing-incidence XRD, which has been demonstrated to be a unique tool in the study of thin films and nanostructures (Pietsch *et al.*, 2004), where it is important to reduce the background coming from the substrate scattering.

**Table 1**

List of the crystal plane reflections available in resonant conditions for two case studies (strained  $\text{In}_{0.38}\text{Ga}_{0.62}\text{As}$  at the In  $L_3$ -edge and  $\text{PbSc}_{0.5}\text{Nb}_{0.5}\text{O}_3$  at the Nb  $L_3$ -edge) given the diffractometer geometry shown in the sketch of Fig. 2.

For each reflection, identified by the  $hkl$  Miller indices, we include the corresponding  $\delta$  and  $\chi$  angles, the interplane spacing ( $d$ ) and the momentum transfer ( $Q = 2\pi/d$ ).

$H$	$K$	$L$	$\delta$ ( $^\circ$ )	$\chi$ ( $^\circ$ )	$d$ ( $\text{\AA}$ )	$Q$ ( $\text{\AA}^{-1}$ )
<b><math>\text{In}_{0.38}\text{Ga}_{0.62}\text{As}</math> at the In <math>L_3</math>-edge</b>						
1	0	1	47.83	46.49	4.10	1.53
1	1	0	49.13	90.00	4.00	1.57
0	0	2	67.86	0.00	2.98	2.11
2	0	0	72.03	90.00	2.83	2.22
1	1	2	88.22	36.68	2.39	2.62
2	1	1	91.15	66.99	2.33	2.70
2	0	2	108.34	46.49	2.05	3.07
2	2	0	112.51	90.00	2.00	3.14
1	0	3	125.10	19.35	1.87	3.36
3	0	1	135.36	72.44	1.80	3.49
3	1	0	136.77	90.00	1.79	3.51
<b><math>\text{PbSc}_{0.5}\text{Nb}_{0.5}\text{O}_3</math> at the Nb <math>L_3</math>-edge</b>						
1	0	0	37.38	90.00	8.16	0.77
0	0	1	37.38	0.00	8.16	0.77
1	1	0	53.89	90.00	5.77	1.09
0	1	1	53.89	45.00	5.77	1.09
1	1	1	67.42	54.74	4.71	1.33
2	0	0	79.71	90.00	4.08	1.54
0	0	2	79.71	0.00	4.08	1.54
2	1	0	91.53	90.00	3.65	1.72
2	1	1	103.42	65.91	3.33	1.89
2	2	0	129.99	90.00	2.89	2.17
3	0	0	148.00	90.00	2.72	2.31
2	2	1	148.00	70.53	2.72	2.31

Moreover, the choice complied with space and weight constraints related to the installation in a rather narrow experimental hutch along with easy transport and maintenance.

### 3.2. Mechanics and performance

The conceptual sketch of Fig. 2 was materialized as shown in Fig. 3(a): the FORTE diffractometer consists of a four-circle HV assembly and two hexapods. The first (large) hexapod works in air, holding the entire vacuum vessel. Its vertical axis rotation ( $Rz$ ) provides the  $\alpha$  arc of the sketch ( $\pm 10^\circ$ ), while the other five degrees of freedom are used to align the diffractometer and centre it on the different possible positions of the incident beam, depending on the mirror configuration chosen. The second (small) hexapod works under vacuum, mounted on the  $\phi$  circle of the goniometer and bears the sample environments, allowing at the same time a fine alignment of the sample surface, independent of the goniometer circles. The volume occupied by the end-station once the vacuum vessel is mounted, as shown in Fig. 3(b), is  $1499 \times 1261 \times 2176$  mm [length (L)  $\times$  width (W)  $\times$  height (H)]: the geometry chosen allowed us to limit the base projection, which was an issue for installation in an already-existing experimental hutch. The total weight of the end-station is about 2050 kg. When the end-station is used for grazing-incidence

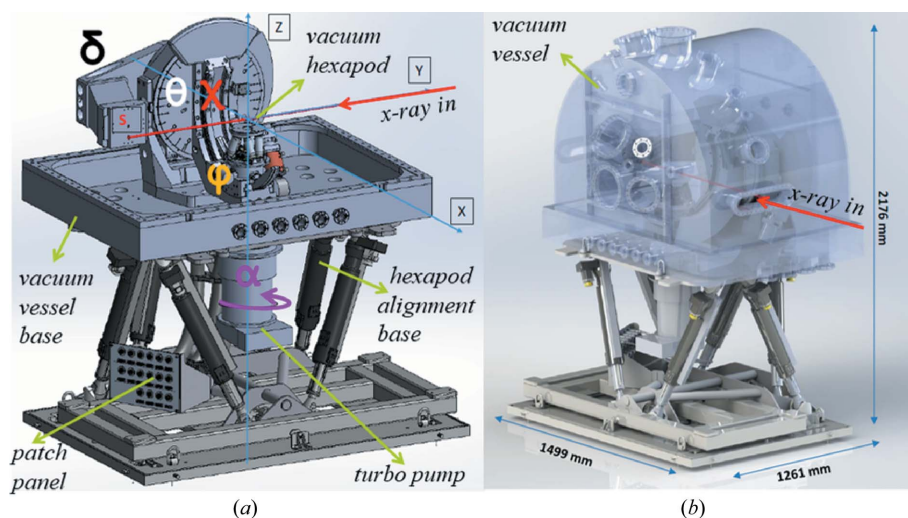


**Figure 3**  
 (a) Illustration of the FORTE diffractometer showing its three main components: the four-circle HV assembly, the large air hexapod alignment base (JORAN) and the HV hexapod sample holder (BORA). (b) Illustration of the diffractometer including a sketch of the vacuum vessel showing the volume occupied by the end-station.

XRD, the entry flange is connected to the beamline by means of a large custom racetrack bellow with (internal) section 372 mm × 70 mm and length around 700 mm. The racetrack bellow, provided by Mewasa (Wangs, Switzerland), allows rotation of the whole diffractometer about the  $\alpha$  vertical rotation axis along with wide translations in the three directions.

The four-circle diffractometer consists of HV-compatible Huber (Rimsting, Germany) circles (references 440.HV for  $\theta$ , 411-X2W2.HV for  $\delta$ , 5202.80.HV for  $\chi$  and 410-X2W1.HV for  $\phi$ ). The circles are actuated by Phytron (Gröbenzell, Germany) HV-compatible stepper motors equipped with Renishaw (Kingswood, UK) absolute encoders. Fig. 4 shows a photograph of the four-circle assembly; the mass of the

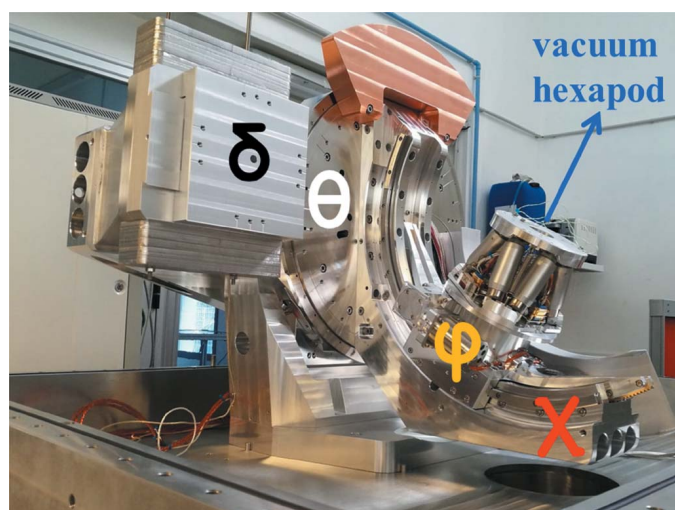


**Figure 4**  
 The four-circle assembly based on Huber HV circles with the BORA hexapod mounted on the  $\phi$  circle.

assembly is 321 kg, and the  $\delta$  arm is optimized for a maximum payload of 12 kg. The large-base hexapod is a customized version of the JORAN hexapod manufactured by the Symétrie company (Nîmes, France); it uses stepper motors and absolute encoders for precision positioning. The possibility of aligning the diffractometer on the different possible beam positions (Ciatto *et al.*, 2016), which are rather distant both along the vertical axis ( $z$ ) and along the axis transverse to the beam ( $x$ ) when focusing mirrors are used, relies on the wide translation range allowed by JORAN (70 mm in  $z$  and 200 mm in  $x$ ). The mass of JORAN is 335 kg and its maximum payload permits it to support the diffractometer, vessel and ancillary instrumentation. The small vacuum hexapod is a standard HV-compatible model (BORA) fabricated by the Symétrie company, featuring direct current (DC)

motors and incremental encoders. Despite its small dimension (base diameter 210 mm, height 141 mm) and mass (4.3 kg), BORA can withstand a maximum payload of 3.5 kg in any direction; this feature, in addition to the location of the centre of rotation of the two hexapod tilts 40 mm above the upper plate, allows the installation of different sample environments.

In order to manage the cables when the HV hexapod moves on the rotatory  $\phi$  plate, a slip ring was installed along the  $\phi$  axis of the goniometer taking advantage of the open base of BORA. The slip ring was manufactured by the RUAG company (Berne, Switzerland). In addition to the hexapod actuator and encoder cables, the slip ring has eight free tracks that can be used for managing sample environment cables, including cables for sample heating, temperature and current measurements, electric field and polarization. Sample environment tracks are centralized into two D-Sub9 connectors fixed on the base of the BORA hexapod. A cable-managing tool consisting of a stainless steel blade guided by an Al housing allows the  $\phi$  + BORA subset to move along the 100° of the  $\chi$  circle segment; the housing maintains the blade when rotating  $\theta$ . Outside the vacuum vessel, the cables coming from the vessel feedthroughs, along with the JORAN air cables, are guided via drag chains to a centralized patch panel installed on the JORAN base. Thanks to lifting eyes installed on the base and upper part of the vacuum vessel and to the customized JORAN base interface, the diffractometer can be easily removed from the SIRIUS experimental hutch as an ensemble and stored in a workshop or laboratory for maintenance and test; reproducibility of the montage is guaranteed by several alignment tools.

The main performance parameters for all diffractometer axes are shown in Table 2. In the table, as also shown in Fig. 3(b), ‘ $z$ ’ represents the vertical direction, ‘ $y$ ’ the direction along the X-ray beam and ‘ $x$ ’ the direction in the horizontal

**Table 2**  
Measured parameters of the FORTE diffractometer.

Axis	Range	Repeatability	Resolution	Precision	Speed
<b>Huber four-circle</b>					
$\theta$	$\pm 180^\circ$	0.0006°	0.0002°	0.0006°	1° s <sup>-1</sup>
$\delta$	-10 / +180°	0.0010°	0.0002°	0.0010°	2° s <sup>-1</sup>
$\chi$	-3 / +100°	0.0007°	0.0002°	0.0009°	0.5° s <sup>-1</sup>
$\phi$	$\pm 180^\circ$	0.0016°	0.0002°	0.0021°	0.37° s <sup>-1</sup>
<b>JORAN hexapod</b>					
$\alpha$ (Rz)	$\pm 10^\circ$	0.0003°	0.0002°	0.0006°	0.17° s <sup>-1</sup>
Tz	-40 / +30 mm	0.001 mm	0.001 mm	0.006 mm	0.93 mm s <sup>-1</sup>
Tx	-95 / +105 mm	0.001 mm	0.001 mm	0.016 mm	2.43 mm s <sup>-1</sup>
Rx	$\pm 2^\circ$	0.0002°	0.0002°	0.0018°	0.09° s <sup>-1</sup>
Ry	$\pm 2^\circ$	0.0002°	0.0002°	0.009°	0.09° s <sup>-1</sup>
<b>BORA hexapod</b>					
Tz	$\pm 10$ mm	0.0001 mm	0.0001 mm	0.0037 mm	1.1 mm s <sup>-1</sup>
Tx	$\pm 20$ mm	0.0008 mm	0.0001 mm	0.013 mm	2.0 mm s <sup>-1</sup>
Ty	$\pm 20$ mm	0.0007 mm	0.0001 mm	0.0107 mm	2.0 mm s <sup>-1</sup>
Rx	$\pm 10^\circ$	0.0002°	0.0001°	0.0079°	1.63° s <sup>-1</sup>
Ry	$\pm 10^\circ$	0.0001°	0.0001°	0.0059°	1.88° s <sup>-1</sup>

plane perpendicular to  $y$ . ‘Tz’ indicates a translation along the  $z$  axis and ‘Rz’ a rotation about the  $z$  axis, the same meaning when switching  $z$  with  $x$  or  $y$ . It is worth remarking on the wide angular range of the four-circle axes and of JORAN Tx and Tz, the very good repeatability of all axes on the full range of the movements (about 0.001° or better for angles and 1  $\mu$ m or better for translations), and the excellent resolutions. With regard to the movement speed, this is relatively high for the  $\theta$ ,  $\delta$  and BORA axes, and lower for the  $\chi$  and  $\phi$  axes due to space/mechanical constraints which drove the choice of the motors. JORAN Rx and Ry also have low speed: since these rotations are usually operated during the alignment phase and not frequently, we chose to favour repeatability over speed. Even though data acquisition is not normally performed in our experiments during the hexapod movements, care was still taken in minimizing the cross coupling while a hexapod axis is operated. The sphere of confusion (SOC) of the diffractometer was measured by using a metrology sphere of mass 3.5 kg mounted on the BORA hexapod (the mass corresponds to the BORA maximum load) and an Orbit digital lever probe by Solartron (Leicester, UK) fixed on the  $\delta$  arm. The  $\delta$  arm was also charged up to its maximum payload (12 kg) for the measurement. The SOC of the diffractometer (including the  $\alpha$  arc) was found to be  $\leq 100$   $\mu$ m at full charge and over the full extension of the diffractometer circles. This SOC value was found to be more than sufficient for all the experiments run until now and it is reasonable

considering the present minimum beam size available at SIRIUS. In order to perform experiments with a smaller beam in the future (a few micrometres in size) the SOC could be reduced considering that it mainly comes from systematic errors due to the  $\chi$  circle guiding and flexion, and exploiting the electronics architecture described below in Section 3.5.

### 3.3. Vacuum vessel and pumping system

The vacuum vessel was provided by the SDMS company (Saint-Romans, France) following a SOLEIL design. It consists of a rectangular base of mass 700 kg and of a half-cylinder-shaped cloche of mass 635 kg, both fabricated

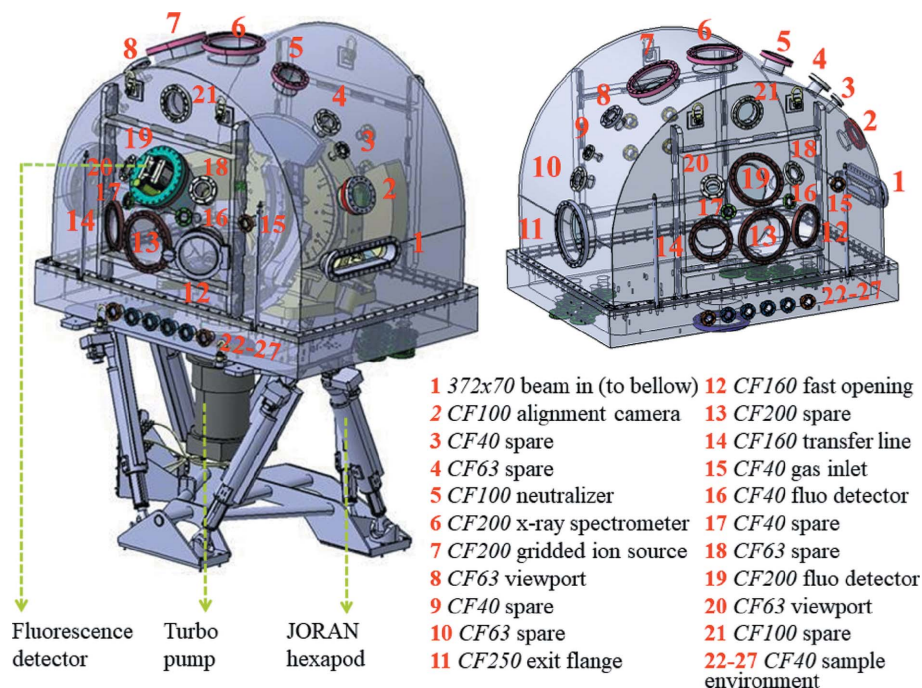


**Figure 5**  
Illustration of the FORTE vacuum vessel including the list of the 27 frontal and top flanges. Another 19 flanges (not included in the list) are located in the rear and bottom sides of the vessel and are dedicated to the electrical feedthroughs of the vacuum motor/encoder cables and of the sample environment/detector electronics, to the turbo pump port, vacuum gauges and pressure safety valve.

flange 19 which allows insertion of a four-element silicon drift detector (SDD) setting the nose in the proximity of the sample. Flange 16 (interchangeable with 17) can be used to set a second SDD further from the sample. Flange 12 is used to mount a viewport equipped with fast opening for manual access to the sample stage, while the in-vacuum sample transfer line can be mounted on flange 14; these two flanges are interchangeable. Flanges 18 and 20, one of which is used to mount a viewport employed to visualize the sample during transfer, are interchangeable too. Flange 2 hosts an optical camera which also assists during sample change, the custom rectangular flange 1 is used for connection to the beamline vacuum through the racetrack bellow described in Section 3.2, and flange 27 for the electrical feedthrough for the heater described below in Section 3.4. Other flanges are dedicated to the installation of new instrumentation in the short and middle term such as electrical feedthroughs and cooling lines for other sample environments (flanges 22–26), a gridded ion source (flange 7) with its neutralizer (flange 5) and a high-resolution vertical X-ray spectrometer (flange 6). Moreover, the diffractometer has been conceived as a versatile, expandable platform and several other spare flanges have been added in order to meet new user needs, equipment and ideas.

All the flanges used for the electrical feedthroughs of the vacuum motor/encoder cables and of the detector electronics, for the vacuum gauges and pressure safety valves have been mounted either at the bottom of the chamber base or at the rear of the vacuum vessel. In fact, these 19 additional flanges do not need to be oriented towards the sample; moreover locating flanges out of the vessel cloche, when possible, makes the opening of the vessel easier for maintenance and/or sample environment and detector change purposes. The flange (CF 200) for connecting a turbo-molecular pump is located at the bottom of the vessel base and allows installation of the pump between the legs of the JORAN hexapod without possibility of collision. We chose an ATH1603 M 200 turbo pump by Pfeiffer (Asslar, Germany) backed by an XDS35i primary pump by Edwards (Burgess Hill, UK), the latter installed on a damper and far from the diffractometer to attenuate vibrations. This pumping system is sufficient to reach HV level: the diffractometer can pass from atmospheric pressure to the  $10^{-7}$  mbar range in a few hours and to the  $10^{-8}$  mbar range in a couple of weeks (if the chamber is not re-opened) without the need of a bake-out. This vacuum performance, obtained with the standard sample environment and detector inserted in the vessel (see Section 3.4), is rather good considering the number of motors installed inside the vacuum vessel. The reachable vacuum level, sufficient for all the experiments carried out until now, could also be improved by adding a second turbo pump on one of the flanges of the upper part of the vessel and/or performing a bake-out of the chamber (the last procedure requiring the removal of sensitive instruments such as the four-element SDD). No issue related to vacuum motor overheating has been experienced to date; nevertheless, the vessel base has been equipped with a flange reserved for a motor water-cooling line in case of

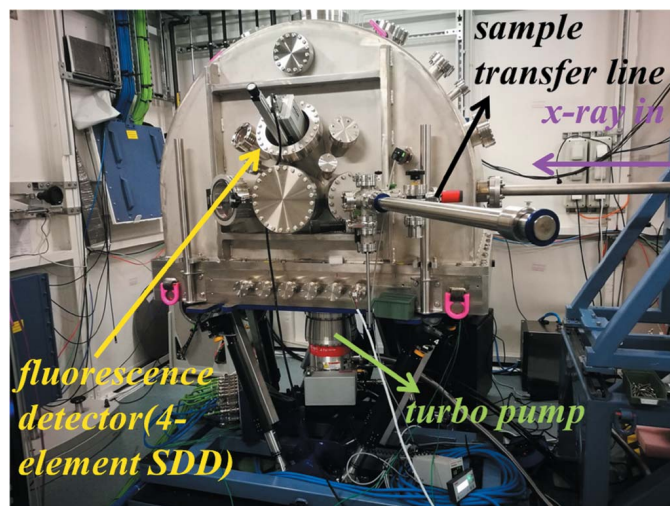


**Figure 6**  
Photograph of the FORTE diffractometer installed in the SIRIUS beamline experimental hutch.

future need, and maximum-temperature watchdogs have been set up.

Fig. 6 shows a photograph of the FORTE diffractometer installed in the SIRIUS beamline experimental hutch with the turbo pump and fluorescence detector installed on the dedicated flanges. One can also notice, on the right side of the figure, the transfer line which allows sample change without breaking the vacuum. The in-vacuum transfer line is based on an all-metal-sealed linear rotary feedthrough equipped with rare-earth magnets on the air and vacuum side to provide the force to ensure a rigid coupling from the handle to the inner shaft. The sample transporter ends with a grabber tool suitable for manipulating flag-style sample plates. The grabber has a matching slit to slide over the sample plate's handle; by twisting the grabber by  $90^\circ$  either way the sample plate can be either held by the grabber or released on a suitable receiver element. All the transfer-line instrumentation is UHV-compatible and was provided by the Ferrovac company (Zürich, Switzerland). The transfer line is also equipped with a cross-shaped pre-chamber featuring a stage of four drawers for flag-style sample plates; this allows one to transfer and measure four samples in a row without opening the pre-chamber. Since the pre-chamber is separated from the main vessel and connected to an additional pump with suitable valves, opening of the main vessel is never needed except for sample environment and detector change.

### 3.4. Sample environment and detectors

The BORA hexapod can host a heating-stage assembly provided by Tectra (Frankfurt, Germany), shown in Fig. 7 (left panel). The heating stage consists of a Boralectric heater (model HTR1001) equipped with twofold Nb foils for heat shielding and a type-K thermocouple mounted inside the heater. It also includes a baseplate and threaded rods with height adjustment, the latter used to position the sample

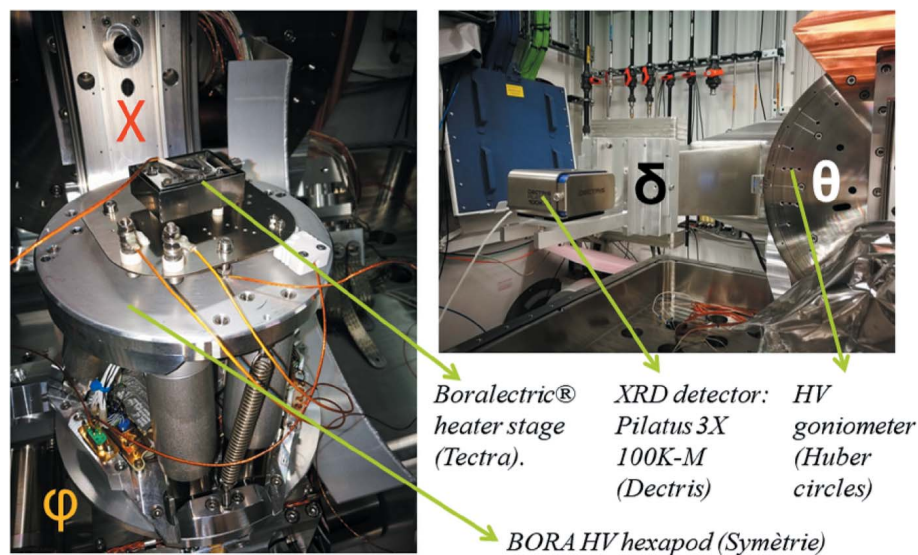


**Figure 7**

Left: photograph of the Boralectric heating stage mounted on the HV hexapod installed on the goniometer. Right: PILATUS3 100K-M detector mounted on the  $\delta$  arm of the FORTE diffractometer.

surface at 40 mm from the BORA plate (*i.e.* the centre of rotation of BORA  $R_x$  and  $R_z$  when the hexapod is on its reference position). A receiver for flag-style sample plates by Ferrovac, fabricated in Mo for better performance at high temperature, is mounted on the Boralectric plate. The circle of the diffractometer and the BORA fine adjustments allow us to easily set the receiver in the face of the sample transporter mounted on its dedicated flange (see Fig. 6). All material and vacuum cabling comply with the HV standard. The heating stage, piloted by a PID controller with autotuning, has been tested with positive results up to 700°C during the diffractometer commissioning. No overheating of the BORA plate and other mechanics nor of the flanges where sensitive elements are located has been sensed. Exploiting the relatively large maximum payload of the BORA hexapod (3.5 kg), we plan to mount several other sample environments in the near future including a sample holder with electrical contacts for measurements under an electric field and more precise temperature/current monitoring at the sample level, a cryostat, and a light variable magnetic field environment based on permanent magnets (Nolle *et al.*, 2012). This new instrumentation is presently under design.

The  $\delta$  arm of the diffractometer allows the installation of several detectors with mass between 0 and 12 kg, using a series of 12 counterweights of 1 kg each for maintaining equilibrium. The detector that we use more frequently is a PILATUS3 100K-M two-dimensional (2D) detector (Fig. 7, right panel) provided by Dectris (Baden, Switzerland). The detector has 172  $\mu\text{m} \times 172 \mu\text{m}$  pixel size, a total detection area of 83.8 mm  $\times$  33.5 mm and a 20 bits dynamic range; it can be positioned within a 160–517 mm distance range from the sample according to the experimental needs, thanks to a sliding support. The PILATUS3 100K-M is designed with an HV-compatible detector head which is inserted in the vessel, and

a separated read-out electronics unit which is located outside (on one of the bottom flanges), the two elements being connected by a cable whose distance has to be kept smaller than 220 cm (including the electrical feedthrough). Nevertheless, this length allows complete coverage of the  $\delta$  circle angular range without any collision of the cables with the mechanics during movements. Water cooling of the detector head is assured by 250 cm-long flexible hoses coupled with suitable cooling feedthroughs. We chose a detector with the ultra low energy calibration option, where the energy threshold can be adjusted between 1.6 and 18 keV; since the energy resolution of the threshold is 500 eV, the recommended working energy range starts around 2.0–2.1 keV and goes up to (and beyond) the maximum energy available at SIRIUS. The use of a robust, sensitive

and fast 2D detector is invaluable when performing grazing-incidence XRD or tender X-ray small-angle scattering (SAXS); however, the PILATUS3 100K-M does not allow us to work down to 1.1 keV. For energy  $< 2$  keV, we presently use a point detector preceded by vacuum slits: the detector is an in-vacuum Peltier-cooled windowless Hamamatsu S2592-04 diode (Hamamatsu City, Japan) with high shunt resistance. The diode electronics consist of a FEMTO DDP-300 current amplifier coupled with an analogue-to-digital converter (ADC) Adlink 2005 (500 kHz) with 16 bit dynamics over 0–10 V. In parallel with the vacuum detectors for XRD, a Bruker XFlash QUAD 5040 four-element SDD fluorescence detector (Billerica, USA) is mounted on flange 19 (see Figs. 5 and 6) for XAS measurements; the detector is equipped with an 8  $\mu\text{m}$ -thick Be vacuum window and it is coupled to four-channel xMAP DXP electronics provided by XIA (Hayward, USA). Finally, the large PILATUS3 1M (Broennimann *et al.*, 2006) detector available at SIRIUS could also be connected to exit flange 11 (Fig. 5) for tender X-ray GISAXS experiments in a He environment.

### 3.5. Electronics, software and control

The diffractometer subsystems (the JORAN and BORA hexapods, and the Huber four-circle assembly) utilize 16 encoded motors to achieve six degrees of freedom (DOF) on diffractometer alignment, six DOF on sample alignment, and a total of five DOF on sample and detector rotations. Performing the necessary movements and/or alignments with low SOC values not only puts a high level of constraints on the mechanical construction, but also on control system requirements. As such, the control system has been implemented using a pre-defined architecture from the REVOLUTION project (Zhang *et al.*, 2015), here based on the high-

performing Delta Tau Powerbrick controller which has recently been integrated as a SOLEIL standard. This controller offers, amongst many features, powerful processing capacity, multi-axis synchronization, encoder processing, virtual/operational space control through kinematic equations, and non-linear trajectories (Abiven *et al.*, 2017). In addition, TANGO (<http://www.tango-controls.org/>) interfacing has been made possible using embedded software libraries written in-house at SOLEIL (Abiven *et al.*, 2017). FORTE control architecture has been developed thanks to a collaboration between SOLEIL, which has provided the high-level TANGO interface, and the Symétrie company, which has provided integrated kinematic routines and system configurations for the hexapods and four-circle subsystems (Abiven *et al.*, 2017) (see Fig. 8).

The implemented architecture uses three Delta Tau Powerbrick LV IMS controllers, each interfacing its own subsystem. The temperatures of the in-vacuum motors are also monitored by an external programmable logic controller (PLC) which interlocks the motion controllers in case of

overheating. Dedicated motor drivers (Phyton) are used for the Huber four-circle system. Fig. 9 shows a more detailed overview of the low-level control architecture. Here, control is classified into two separate schemes:

(a) Powerbrick N 1 (BORA control system, multi-axial cascaded control): all six motors are separately driven and controlled with motor phase currents at 16 kHz and motor positional servo control at 4 kHz, all of which move in synchronized trajectories using model-based kinematics. TANGO control is exerted via the shared memory using dedicated libraries.

(b) Powerbrick N 3 + 2 (JORAN + Huber control system, multi-axial cascaded control over two controllers): synchronized control of the JORAN and Huber four-circle systems is achieved via the MACRO bus [an open protocol developed by Delta Tau that is used for real-time motion (Abiven *et al.*, 2017)] between two Powerbrick controllers. This allows the master controller (No. 3) to perform the closed-loop servo (at 4 kHz) and synchronized multi-axial trajectory calculations (with kinematics at 1 kHz) for the JORAN and Huber systems. TANGO control is exerted via the master controller. Synchronized motion of the Huber assembly and JORAN allows for two major advantages:

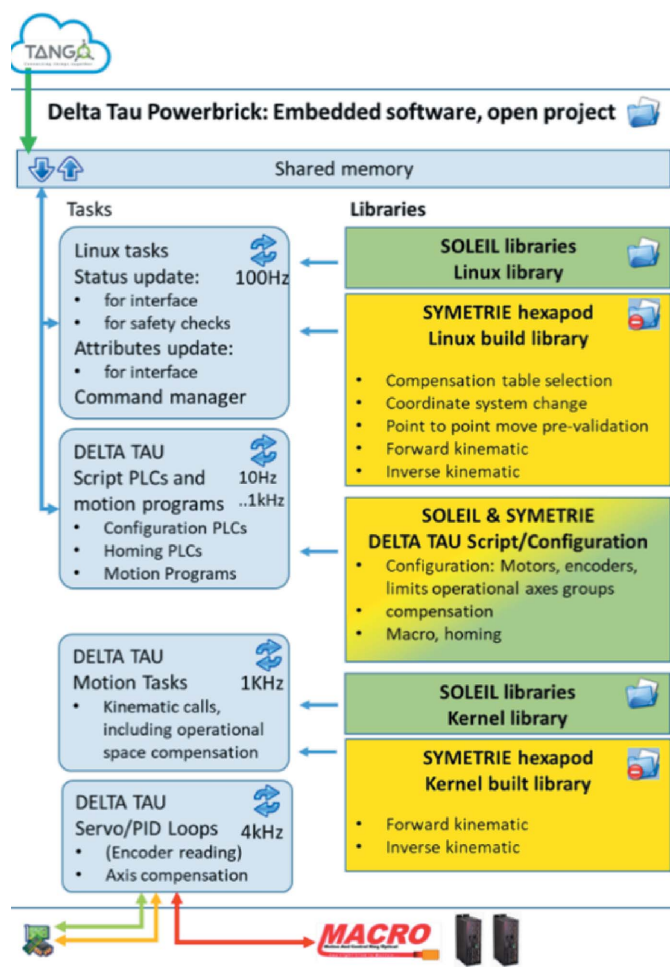


Figure 8 Controller-embedded software. In the SOLEIL–Symétrie collaboration, SOLEIL has provided TANGO interfacing libraries (marked green), while Symétrie has provided kinematic routines and system configurations (marked yellow).

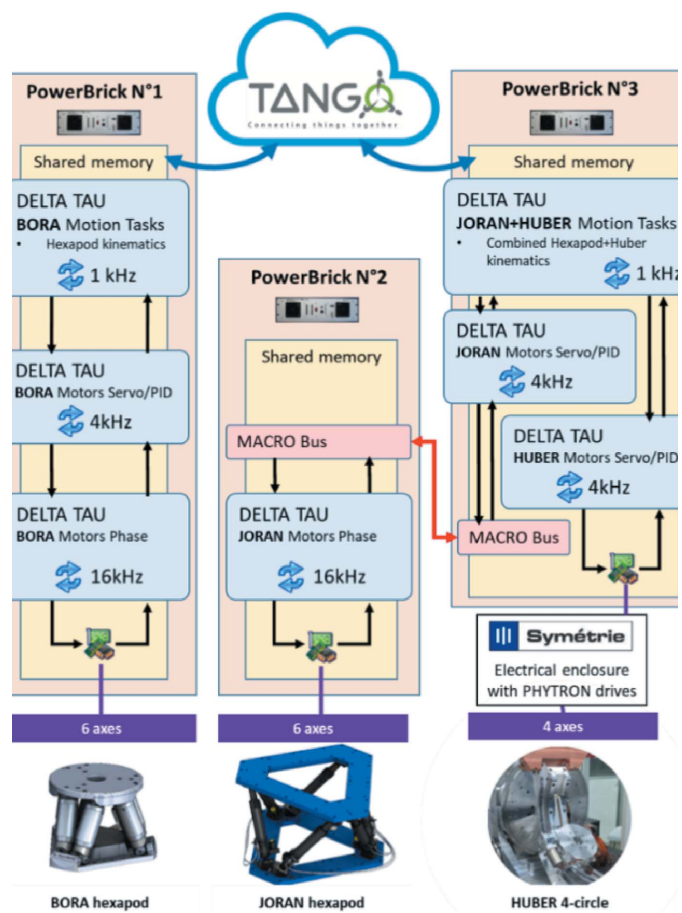


Figure 9 Low-level system control architecture.

(i) The JORAN platform can also be used for sample and detector movements, thus adding a fifth rotational DOF to the Huber four-circle system (the  $\alpha$  angle defined in Section 3.1).

(ii) Repeatability errors of the Huber four-circle assembly can be corrected for with the JORAN platform using compensation tables (in a feedforward manner), and thus reducing the SOC of detector and sample circular motions.

The second control scheme (b) works well when using six-DOF hexapods for motion error compensation. This scheme can be further scaled up to synchronize all Powerbricks (Nos. 1 + 2 + 3) using the MACRO bus; this will allow the use of the BORA hexapod (instead of JORAN) to improve the diffractometer SOC via compensation tables. The use of BORA for this purpose is more convenient since its movements are faster and they do not induce a displacement of the diffractometer centre with respect to the incident-beam position. These synchronization possibilities and the SOC improvement will be key for future experiments with smaller X-ray beams (see Section 5).

The TANGO control software can be further employed using a high-level environment developed at SOLEIL (called SPYC) which provides a friendly and versatile interface to the users. The SPYC platform is written in the Python programming language and allows one to use commands to move and scan several motors at the same time (undulator gap, monochromator and diffractometer axes), and to write scripts and macros for automatic acquisition.

## 4. Experimental applications

In this section we show selected examples of the results of the first commissioning and collaborative experiments recently performed using the FORTE diffractometer, which was commissioned at the SIRIUS beamline in the first semester of 2018; it is now open to the public user programme. Here we present data relative to tender X-ray DAFS experiments, tender X-ray grazing-incidence XAS and XRD reciprocal-space mapping. The use of the end-station for other experiments, such as tender X-ray SAXS/GISAXS and resonant XRR, is also possible and some of them are expected in the near future. It is worth remarking that this section exclusively aims at presenting the potential of the new HV diffractometer for experiments; quantitative analysis of the results presented (which is in progress) is out of the scope of this paper.

### 4.1. Tender X-ray DAFS

$\text{PbSc}_{0.5}\text{Nb}_{0.5}\text{O}_3$  (PSN) is a perovskite oxide ( $\text{ABO}_3$ ) whose properties switch from ferroelectric (FE) to relaxor or anti-ferroelectric according to the degree of ordering of Sc and Nb atoms on the B site (FE when partially ordered, anti-FE when perfectly ordered and relaxor when disordered) (Malibert *et al.*, 1997). Correlated anti-parallel displacements of the Pb cations as well as oxygen octahedra rotations can influence the properties of the material, which is interesting for technological applications in filters, sensors/actuators and antennas. The coexistence of ordered and disordered regions within the

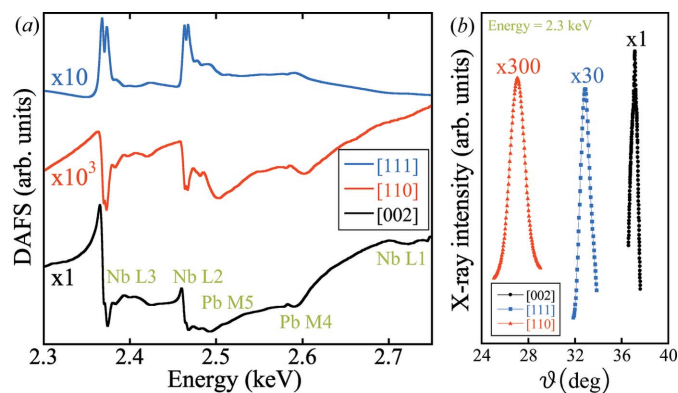


**Figure 10**

(a) DAFS spectra taken on a  $\text{PbSc}_{0.5}\text{Nb}_{0.5}\text{O}_3$  sample using three different reflections ([002], [110], [111]), spanning the energy range of the Nb L-edges and the Pb M-edges. The three DAFS spectra are multiplied by a factor (given on the left of the figure) in order to be plotted on the same scale. (b) XRD  $\theta$ - $2\theta$  scans performed around the three crystal plane reflections at energy 2.3 keV.

same sample is also possible. When these crystals are studied with XRD, different reflections are visible: some of them are pure structural reflections (such as the [002] one), others are superstructure reflections arising from the ordered alternation of Sc and Nb planes (such as the [110] one), others again are thought to reflect chemical order (Sc, Nb) along a crystallographic direction plus the anti-parallel cationic displacements along the same direction (such as the [111] one). Fig. 10(a) shows three DAFS spectra taken using the [002], [110] and [111] reflections in an energy interval spanning the L-absorption edges of Nb and the M-edges of Pb; Fig. 10(b) shows XRD  $\theta$ - $2\theta$  scans performed around the three crystal plane reflections at energy 2.3 keV where the Bragg peaks are visible. Quantitative analysis of the DAFS spectra taken at the different structure and superstructure reflections will allow us to shed some light on the relative fraction and nature of the chemically ordered regions. In particular, DAFS is suitable for understanding how the single elements participate in a specific superstructural order and if the local structure of the atoms involved in that superstructural order is different from the average one. Together with XAS data obtained at the Nb L-edges and Sc K-edge on the same samples (not shown), these experimental results will be very useful to clarify the correlation between short-range order, local density of states and relaxor properties in PSN. We note here that the use of the Nb L<sub>3</sub>-edge makes our probe sensitive to orbitals with *d* symmetry, which is particularly important since Nb has 4*d* electrons in the valence band and these electrons are involved in bonding with O 2*p* electrons. Finally, it is also worth remarking that the use of a four-circle diffractometer with large angular range (including for  $\chi$ ) is here mandatory to explore the different reflections used in the DAFS study (see Table 1, bottom part).

Another scientific case which can benefit from tender X-ray DAFS is the study of strong correlated functional oxide systems showing a metal-insulator transition (MIT). In  $\text{SrVO}_3$  (SVO) (Yoshimatsu *et al.*, 2010; Gu *et al.*, 2014; Fouchet *et al.*,

2016, 2018), which is a paramagnetic metal in the bulk, the MIT can be induced by decreasing the thickness to a few nanometres. Furthermore, the MIT can be influenced by the strain imposed on the thin epitaxial SVO layer by different kinds of substrates such as a stressful SrTiO<sub>3</sub> (STO) or a more lattice-matched (La,Sr)(Al,Ta)O<sub>3</sub> (LSAT); the presence of a cap layer (STO or LaAlO<sub>3</sub>, LAO) can also stress the metallic SVO layer. Hence, the study of the effects of strains from above or below on the local structure of all elements in the SVO layer is crucial to disentangle the pure dimensional reduction effect from strain effects in sandwiched SVO layers. It is highly relevant to correlate these effects with the electronic structure and transport properties. If on the one hand the local environment of V atoms (occupying the *B* site of the perovskite) can be accessed via XAS, on the other hand a study of the local structure and local density of states around the Sr atoms (occupying the *A* site) as a function of the SVO layer thickness requires the combined chemical and crystallographic selectivity of DAFS, due to the presence of Sr in both STO and LSAT substrates. The use of grazing-incidence (GI) XAS is not an option considering the presence of a nanometric cap layer. In Fig. 11 we show a DAFS spectrum of a LAO(3 nm)/SVO(35 nm)/STO heterostructure in the region of the Sr *L*<sub>3</sub>- and *L*<sub>2</sub>-absorption edges, selecting the [001] crystal plane reflection of SVO. As shown in Fig. 11 (inset), the SVO [001] reflection can be separated as a shoulder on the right side of the intense STO [001] substrate peak in an XRD  $\theta$ - $2\theta$  scan. The DAFS Sr *L*<sub>3</sub>-edge spectra have very high quality; simulating them *ab initio* based on model strain structures will be very helpful in monitoring and understanding the evolution of the Sr local density of unoccupied states and local structure as a function of the sample thickness, through the MIT. We note once more that access to the Sr *L*<sub>3</sub>- and *L*<sub>2</sub>-absorption edges is important because this allows us to probe final states with *d* symmetry, relevant in the chemical

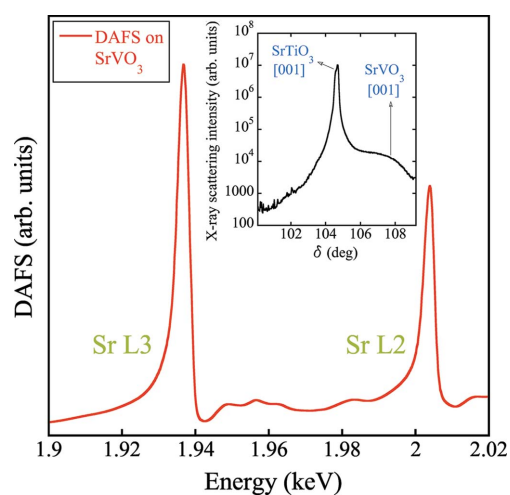


**Figure 11**  
Sr *L*<sub>3</sub>-edge DAFS spectrum of a 35 nm SrVO<sub>3</sub> layer sandwiched in a LaAlO<sub>3</sub>/SrVO<sub>3</sub>/SrTiO<sub>3</sub> structure; inset: XRD  $\theta$ - $2\theta$  scan around the SrTiO<sub>3</sub> [001] substrate peak showing the SrVO<sub>3</sub> [001] shoulder on the high-angle side.

bonds. Since these edges are located at rather low energies in the tender X-ray region (1.94 and 2.0 keV), large  $\delta$  angles (between 100° and 120°) are necessary; the DAFS experiment is possible thanks to the wide  $\delta$  range made available by the FORTE diffractometer. For uncapped samples, the SVO [100] reflection, accessible in GI, could also be used for DAFS thanks to the possibility of switching from bulk to surface geometry anticipated in Section 3.1: choosing a GI-DAFS geometry would permit one to enhance the diffraction signal of the SVO layer with respect to the substrate one.

#### 4.2. Tender X-ray grazing-incidence XAS

In parallel with tender XRD and DAFS, the FORTE diffractometer can also be used for XAS experiments in the same energy range, thanks to the four-element SDD described in Section 3, which allows measurement of even ultra high dilute systems. In some cases, when the sample geometry and Bragg angles at play allow it and self-absorption is not an issue, XAS measurements can also be performed simultaneously to DAFS resulting in time saving (Ciatto *et al.*, 2018). In other cases, it may be interesting to choose a specific incidence angle for the XAS measurements; this is often a requirement in experiments on nanostructures, where confining the X-ray probe in a near-surface region using a subcritical grazing angle allows reduction of the signal background generated from fluorescence lines originating from the substrate or buffer layers. In Fig. 12 we present XRR and P *K*-edge XAS spectra taken on a self-assembled monolayer P-containing molecule, the octadecylphosphonic acid (ODPA), deposited on Si substrate. This molecule is interesting for the monolayer contact doping process of Si and related nanostructures (Arduca *et al.*, 2016), in which a subsequent annealing forces P diffusion into the structure beneath the molecule; doping of a nanostructured semiconductor is in fact a key issue for future nanoelectronics. As

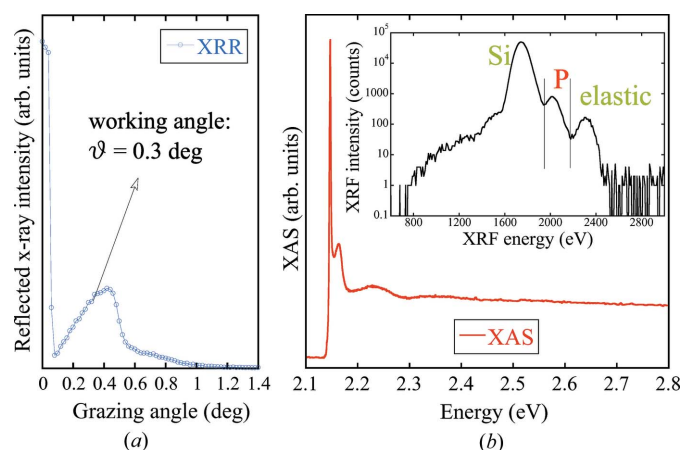


**Figure 12**  
(a) XRR curve in the vicinity of the P *K*-edge taken on an ODPA monolayer deposited on Si substrate. (b) P *K*-edge GI-XAS spectrum of the same sample taken in fluorescence mode with the SDD; the inset shows a fluorescence spectrum taken at 2.3 keV in GI, where it is possible to discriminate the P *K* $\alpha$  peak from the Si *K* $\alpha$  and elastic peaks.

preliminary information for the monolayer contact doping process, it is interesting to know the local structure of P in the as-deposited layers and the interaction and bonding with the Si substrate. A study of the local environment of P by fluorescence-mode XAS on this system is challenging since, even if the P  $K\alpha$  and Si  $K\alpha$  lines are separated by  $\sim 300$  eV and the energy resolution of the SIRIUS SDD is  $\sim 130$  eV, the strong Si fluorescence background coming from the substrate would hinder any XAS measurements at the P  $K$ -edge in wide incident-angle geometry. In fact, the fluorescence detector would saturate before having a sufficiently high P  $K\alpha$  count rate. Using the FORTE diffractometer, we can perform precise reflectivity curves to determine the critical angle of the sample, using the HV PILATUS3 100K-M detector for measuring the reflected signal [Fig. 12(a)]. Working at incidence angles smaller than the critical one for total reflection (we chose  $\theta = 0.3^\circ$  in this case) allows limitation of the X-ray penetration to a few nm beneath the surface, enhancing the monolayer contribution and improving the P  $K\alpha$ /Si  $K\alpha$  count rate ratio and signal-to-noise ratio. This setup allows us to separate the P  $K\alpha$  signal located between the Si  $K\alpha$  and elastic peaks in a fluorescence spectrum taken after the edge [Fig. 12(b) inset], and to obtain from its integration high-quality P  $K$ -edge XAS spectra of the deposited monolayer ODPa molecule [Fig. 12(b) main image].

#### 4.3. Reciprocal-space mapping

The availability of an in-vacuum 2D detector mounted on the  $\delta$  arm of the FORTE diffractometer opens the possibility of acquiring XRD reciprocal-space maps (RSMs) in a fast way, in particular at energies corresponding to resonances of interest in the tender X-ray region. RSMs are very useful to evaluate strain in epitaxial systems and can be associated with multiwavelength anomalous diffraction (MAD) (Hodeau *et al.*, 2001) to correlate specific strain regions with concentration gradients of the chemical elements (Létoublon *et al.*, 2004). Furthermore, in epitaxial templates, RSMs allow one to easily discriminate different diffraction peaks coming from the active layer, buffers and substrate, and to select the desired one for a DAFS analysis, even in cases where the same chemical element is present in more than one layer of the template. This is the case shown in Fig. 13(a), where we analysed InP wurtzite (wz) [001] nanowires (NWs) grown on InP zincblende (zb) [111] substrate at an energy (2.2 keV) just above the P  $K$ -edge. Despite the low incidence energy, the wz [002] peak ( $\delta = 112.07^\circ$ ) and the [111] zb one ( $\delta = 112.79^\circ$ ) are still rather close to each other. Nevertheless, the RSM of Fig. 13(a) allows separation of the two diffraction spots.

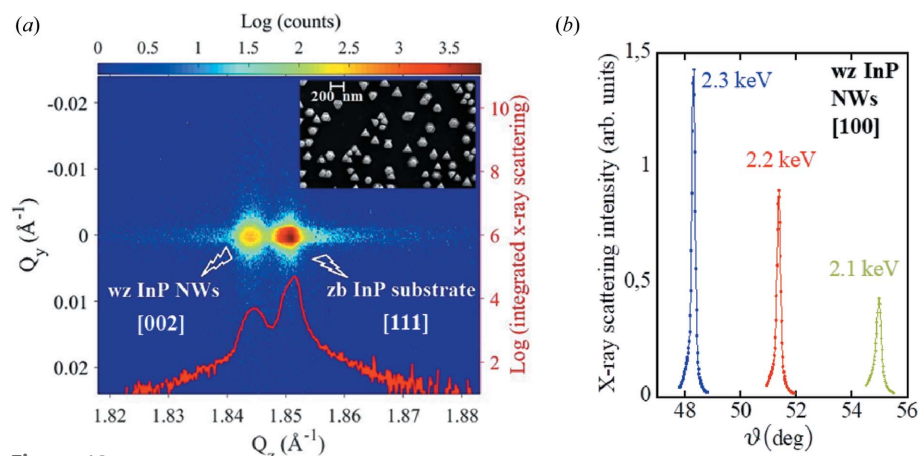


**Figure 13**  
(a) RSM taken at 2.2 keV on InP wz nanowires grown on InP zb substrate using the PILATUS3 100K-M detector. The close XRD spots of the wz [002] reflection and the zb [111] one can be separated in the map. A (red) curve representing the count rate integrated along the  $Q_y$  direction is superposed on the RSM.  $Q_y$  is the component of the momentum transfer in the  $y$  direction (transversal to the X-ray beam),  $Q_z$  is the component perpendicular to the surface. The inset shows a scanning electron microscopy image of the sample. (b) XRD  $\theta$ - $2\theta$  scans performed in GI around the [100] reflection of the InP wz nanowires for different energies around the P  $K$ -edge.

Another strategy to discriminate the structure of the NWs from that of the substrate is to choose the wz [100] reflection; this reflection ( $\delta = 103.58^\circ$ ) is accessible in grazing incidence using the FORTE configuration shown in Fig. 2(b) and, as one can see from the  $\theta$ - $2\theta$  scans of Fig. 13(b), has no substrate reflection immediately nearby.

#### 5. Upgrade path

The upgrade path foreseen for the FORTE end-station will follow two lines. The first line consists of the aforementioned completion of the sample environment and detector setups, beyond the basic functionality already implemented. This will include the installation of a sample holder with electrical contacts for measurements under an electric field, interesting for the analysis of ferroelectric/piezoelectric samples, a magnetic field environment for XMCD and XRMS measurements, a cryostat and, finally, a vertical high-resolution tender X-ray spectrometer with Von Hamos geometry (Anklamm *et al.*, 2014) for coupling XAS with X-ray emission spectroscopy (XES) in order to study the occupied/unoccupied local density of states and 'local' band gaps in semiconductors (Amidani *et al.*, 2014).

The second line will occur in parallel with the upgrade of the SOLEIL ring towards an MBA lattice in the near future. The foreseen two orders of magnitude increase in brilliance will bring about an equivalent increase in the fraction of transverse coherence of the X-ray beam and, as a consequence, of the coherent photon flux available at the beamlines. Moreover, in the case of the SOLEIL ring, the performance improvement will be particularly impressive in the tender X-ray region and for our kind of undulator source. This will pave the way for the use of the FORTE end-station for CDI in Bragg geometry (Pfeifer *et al.*, 2006). It is worth remarking here that progress in the development of robust single-

photon-counting 2D detectors working in the tender X-ray region with a pixel size smaller than in the PILATUS (for example CMOS-based) is expected in the near future. These new detectors would prevent lower resolution in speckle sampling due to the limited maximum sample–detector distance and consequent reduced speckle size.

The possibility of using a smaller and intense X-ray beam will call for an improvement of the four-circle diffractometer SOC. The control architecture based on synchronized Delta Tau units described in Section 3.5 opens up exciting perspectives in this sense. In fact, since we know from the manufacturer that the SOC errors mainly originate from the  $\chi$  circle guiding and flexion, a full metrology of these systematic errors could be carried out and the results injected as input to our control system to correct them in real time using synchronized movements of one of the hexapods (e.g. BORA).

## 6. Conclusions

We have presented a high-vacuum diffractometer for tender X-ray diffraction and spectroscopy recently installed at the SIRIUS beamline of the French national synchrotron source (Synchrotron SOLEIL). This new end-station, called FORTE, is highly versatile and opens exciting perspectives to users offering different techniques in the tender X-ray range: (GI)XRD, DAFS, (GI)XAS, XRR, GISAXS. The diffractometer allows investigation of bulk samples as well as of surfaces, interfaces and nanostructures; it has a sufficient number of circles and extended angular ranges to cover a large volume in reciprocal space and can work in the  $10^{-8}$  mbar vacuum range despite the presence of several in-vacuum motors. FORTE was commissioned in the first semester of 2018 and is now open to the public user programme. Selected results of the first experiments performed have been presented as examples of its present potential. Finally, an appealing upgrade path of the end-station is foreseen in the near future.

## Acknowledgements

We thank all our colleagues at SOLEIL (in particular from the vacuum, alignment, detector, optics, electronics and software group) who contributed to the conception and installation of the FORTE diffractometer. We thank the Symétrie company (Nîmes, France), and in particular O. Dupuy, for the excellent work in the design and assembly of the diffractometer system based on our conceptual idea. GC thanks P. Morin (SOLEIL) for advice during the project writing phase, J. Larsson (MAX IV) for useful discussion. GC also thanks H. Renevier, A. Deschamps (Grenoble-INP) and the SOLEIL Scientific Advisory Committee (SAC) for recommending his applications for funding. Finally, we thank M. De Luca (University of Basel), A. Polimeni (University of Rome La Sapienza), C. Jagadish (Australian National University), D. De Salvador and F. Sgarbossa (University of Padova) for providing some of the samples used in the experiments presented in the work.

## Funding information

The project was funded by the Swedish Research Council (Vetenskapsrådet MAX IV–SOLEIL collaboration) and the Île-de-France region (project ‘FORTE’, DIM OXYMORE).

## References

- Abiven, Y. M., Aubert, N., Ciatto, G., Engblom, C., Fontaine, P., Zhang, S., L’Hostis, A., Noire, P., Dupuy, O. & Roux, T. (2017). *Proceedings of the 16th International Conference on Accelerator and Large Experimental Physics Control Systems (ICALPECS 2017)*, Barcelona, Spain, October 2017, pp. 380–384.
- Abrudan, R., Brüßing, F., Salikhov, R., Meermann, J., Radu, I., Ryll, H., Radu, F. & Zabel, H. (2015). *Rev. Sci. Instrum.* **86**, 063902.
- Amidani, L., Ciatto, G., Boscherini, F., Filippone, F., Mattioli, G., Alippi, P., Bondino, F., Polimeni, A., Capizzi, M. & Amore Bonapasta, A. (2014). *Phys. Rev. B*, **89**, 085301.
- Anklamm, L., Schlesiger, C., Malzer, W., Grötzsch, D., Neitzel, M. & Kanngießer, B. (2014). *Rev. Sci. Instrum.* **85**, 053110.
- Arduca, E., Mastromatteo, M., De Salvador, D., Seguni, G., Lenardi, C., Napolitani, E. & Perego, M. (2016). *Nanotechnology*, **27**, 075606.
- Bao, Y., Zhao, C., Li, Y. & Yun, X. (2018). *Sci. Rep.* **8**, 13523.
- Beale, T. A. W., Hase, T. P. A., Iida, T., Endo, K., Steadman, P., Marshall, A. R., Dhesi, S. S., van der Laan, G. & Hatton, P. D. (2010). *Rev. Sci. Instrum.* **81**, 073904.
- Beutier, G., Marty, A., Livet, F., van der Laan, G., Stanescu, S. & Bencok, P. (2007). *Rev. Sci. Instrum.* **78**, 093901.
- Bloch, J. M. (1985). *J. Appl. Cryst.* **18**, 33.
- Boichot, R., Tian, L., Richard, M. I., Crisci, A., Chaker, A., Cantelli, V., Coindeau, S., Lay, S., Ouled, T., Guichet, C., Chu, M. H., Aubert, N., Ciatto, G., Blanquet, E., Thomas, O., Deschamps, J. L., Fong, D. D. & Renevier, H. (2016). *Chem. Mater.* **28**, 592–600.
- Broennimann, Ch., Eikenberry, E. F., Henrich, B., Horisberger, R., Huelsen, G., Pohl, E., Schmitt, B., Schulze-Briese, C., Suzuki, M., Tomizaki, T., Toyokawa, H. & Wagner, A. (2006). *J. Synchrotron Rad.* **13**, 120–130.
- Brück, S., Bauknecht, S., Ludescher, B., Goering, E. & Schütz, G. (2008). *Rev. Sci. Instrum.* **79**, 083109.
- Bunk, O. & Nielsen, M. M. (2004). *J. Appl. Cryst.* **37**, 216–222.
- Busing, W. R. & Levy, H. A. (1967). *Acta Cryst.* **22**, 457–464.
- Ciatto, G., Chu, M. H., Fontaine, P., Aubert, N., Renevier, H. & Deschamps, J. L. (2016). *Thin Solid Films*, **617**, 48–54.
- Ciatto, G., Pettinari, G. & Polimeni, A. (2018). *J. Appl. Phys.* **124**, 165709.
- Desjardins, K., Pomorski, M. & Morse, J. (2014). *J. Synchrotron Rad.* **21**, 1217–1223.
- Dyadkin, V., Pattison, P., Dmitriev, V. & Chernyshov, D. (2016). *J. Synchrotron Rad.* **23**, 825–829.
- Einfeld, D. (2014). *Synchrotron Radiat. News*, **27**(6), 4–7.
- Enquist, H., Jurgilaitis, A., Jarnac, A., Bengtsson, A. U. J., Burza, M., Curbis, F., Disch, C., Ekström, J. C., Harb, M., Isaksson, L., Kotur, M., Kroon, D., Lindau, F., Mansten, E., Nygaard, J., Persson, A. I. H., Pham, V. T., Rissi, M., Thorin, S., Tu, C.-M., Wallén, E., Wang, X., Werin, S. & Larsson, J. (2018). *J. Synchrotron Rad.* **25**, 570–579.
- Feidenhans’l, R. (1989). *Surf. Sci. Rep.* **10**, 105–188.
- Fontaine, P., Ciatto, G., Aubert, N. & Goldmann, M. (2014). *Sci. Adv. Mater.* **6**, 2312–2316.
- Fouchet, A., Allain, M., Bérini, B., Popova, E., Janolin, P.-E., Guiblin, N., Chikoidze, E., Scola, J., Hrabovsky, D., Dumont, Y. & Keller, N. (2016). *Mater. Sci. Eng. B*, **212**, 7–13.
- Fouchet, A., Rault, J. E., Allain, M., Bérini, B., Rueff, J.-P., Dumont, Y. & Keller, N. (2018). *J. Appl. Phys.* **123**, 055302.
- Fuchs, M. R., Pradervand, C., Thominet, V., Schneider, R., Panepucci, E., Grunder, M., Gabadinho, J., Dworkowski, F. S. N., Tomizaki, T., Schneider, J., Mayer, A., Curtin, A., Olieric, V., Frommherz, U.,

- Kotrlé, G., Welte, J., Wang, X., Maag, S., Schulze-Briese, C. & Wang, M. (2014). *J. Synchrotron Rad.* **21**, 340–351.
- Fuoss, P. H. & Robinson, I. K. (1984). *Nucl. Instrum. Methods Phys. Res.* **222**, 171–176.
- Grabis, J., Nefedov, A. & Zabel, H. (2003). *Rev. Sci. Instrum.* **74**, 4048–4051.
- Gu, M., Wolf, S. A. & Lu, J. W. (2014). *Adv. Mater. Interfaces*, **1**, 1300126.
- Hawthorn, D. G., He, F., Venema, L., Davis, H., Achkar, A. J., Zhang, J., Sutarto, R., Wadati, H., Radi, A., Wilson, T., Wright, G., Shen, K. M., Geck, J., Zhang, H., Novák, V. & Sawatzky, G. A. (2011). *Rev. Sci. Instrum.* **82**, 073104.
- Hodeau, J.-L., Favre-Nicolin, V., Bos, S., Renevier, H., Lorenzo, E. & Berar, J.-F. (2001). *Chem. Rev.* **101**, 1843–1867.
- Huang, Z., Bartels, M., Xu, R., Osterhoff, M., Kalbfleisch, S., Sprung, M., Suzuki, A., Takahashi, Y., Blanton, T. N., Salditt, T. & Miao, J. (2015). *Nat. Mater.* **14**, 691–695.
- Jaouen, N., Tonnerre, J.-M., Kapoujian, G., Taunier, P., Roux, J.-P., Raoux, D. & Sirotti, F. (2004). *J. Synchrotron Rad.* **11**, 353–357.
- Ju, G., Highland, M. J., Yanguas-Gil, A., Thompson, C., Eastman, J. A., Zhou, H., Brennan, S. M., Stephenson, G. B. & Fuoss, P. H. (2017). *Rev. Sci. Instrum.* **88**, 035113.
- Kitegi, C., Briquez, F., Couprie, M.-E., El Ajjouri, T., Filhol, J.-M., Tavakoli, T. & Vétéran, J. (2010). *Proceedings of IPAC'10, Kyoto, Japan*, p. 3099.
- Lee, J. H., Tung, I. C., Chang, S.-H., Bhattacharya, A., Fong, D. D., Freeland, J. W. & Hong, H. (2016). *Rev. Sci. Instrum.* **87**, 013901.
- Létoublon, A., Favre-Nicolin, V., Renevier, H., Proietti, M. G., Monat, C., Gendry, M., Marty, O. & Priester, C. (2004). *Phys. Rev. Lett.* **92**, 186101.
- Lohmeier, M. & Vlieg, E. (1993). *J. Appl. Cryst.* **26**, 706–716.
- Malibert, C., Dkhil, B., Kiat, J., Durand, D., Béar, J. F. & Spasojevic, A. (1997). *J. Phys. C Condens. Matter*, **9**, 7485.
- McBride, E. E., Krygier, A., Ehnes, A., Galtier, E., Harmand, M., Konopková, Z., Lee, H. J., Liermann, H.-P., Nagler, B., Pelka, A., Rodel, M., Schropp, A., Smith, R. F., Spindloe, C., Swift, D., Tavella, F., Toleikis, S., Tschentscher, T., Wark, J. S. & Higginbotham, A. (2019). *Nat. Phys.* **15**, 89–94.
- Murphy, B. M., Greve, M., Runge, B., Koops, C. T., Elsen, A., Stettner, J., Seeck, O. H. & Magnussen, O. M. (2014). *J. Synchrotron Rad.* **21**, 45–56.
- Nemoz, C., Ropars, V., Frit, P., Gontier, A., Drevet, P., Yu, J., Guerois, R., Pitois, A., Comte, A., Delteil, C., Barboule, N., Legrand, P., Bacconnais, S., Yin, Y., Tadi, S., Barbet-Massin, E., Berger, I., Le Cam, E., Modesti, M., Rothenberg, E., Calsou, P. & Charbonnier, J. B. (2018). *Nat. Struct. Mol. Biol.* **25**, 971–980.
- Nicklin, C., Arnold, T., Rawle, J. & Warne, A. (2016). *J. Synchrotron Rad.* **23**, 1245–1253.
- Nolle, D., Weigand, M., Audehm, P., Goering, E., Wiesemann, U., Wolter, C., Nolle, E. & Schütz, G. (2012). *Rev. Sci. Instrum.* **83**, 046112.
- Nowak, D. E., Blasini, D. R., Vodnick, A. M., Blank, B., Tate, M. W., Deyhim, A., Smilgies, D.-M., Abruña, H., Gruner, S. M. & Baker, S. P. (2006). *Rev. Sci. Instrum.* **77**, 113301.
- Pfeifer, M. A., Williams, G. J., Vartanyants, I. A., Harder, R. & Robinson, I. K. (2006). *Nature*, **442**, 63–66.
- Pietsch, U., Holý, V. & Baumbach, T. (2004). *High-Resolution X-ray Scattering. From Thin Films to Lateral Nanostructures*. New York: Springer Verlag.
- Seeck, O. H., Deiter, C., Pflaum, K., Bertam, F., Beerlink, A., Franz, H., Horbach, J., Schulte-Schrepping, H., Murphy, B. M., Greve, M. & Magnussen, O. (2012). *J. Synchrotron Rad.* **19**, 30–38.
- Smilgies, D.-M., Boudet, N., Struth, B. & Kononov, O. (2005). *J. Synchrotron Rad.* **12**, 329–339.
- Staub, U., Scagnoli, V., Bodenthin, Y., García-Fernández, M., Wetter, R., Mulders, A. M., Grimmer, H. & Horisberger, M. (2008). *J. Synchrotron Rad.* **15**, 469–476.
- Strempler, J., Francoual, S., Reuther, D., Shukla, D. K., Skaugen, A., Schulte-Schrepping, H., Kracht, T. & Franz, H. (2013). *J. Synchrotron Rad.* **20**, 541–549.
- Takeuchi, T., Chainani, A., Takata, Y., Tanaka, Y., Oura, M., Tsubota, M., Senba, Y., Ohashi, H., Mochiku, T., Hirata, K. & Shin, S. (2009). *Rev. Sci. Instrum.* **80**, 023905.
- Thorkildsen, G., Mathiesen, R. H. & Larsen, H. B. (1999). *J. Appl. Cryst.* **32**, 943–950.
- Vlieg, E. (1998). *J. Appl. Cryst.* **31**, 198–203.
- Yoshimatsu, K., Okabe, T., Kumigashira, H., Okamoto, S., Aizaki, S., Fujimori, A. & Oshima, M. (2010). *Phys. Rev. Lett.* **104**, 147601.
- Zhang, S., Abiven, Y.-M., Blache, F., Corruble, D., Kheffafa, C. & Minolli, S. (2015). *Proceedings of the 15th International Conference on Accelerator and Large Experimental Physics Control Systems (ICALEPCS 2015)*, Melbourne, Australia, October 2015, pp. 201–204.